


Operating regimes of cavity solitons by virtue of a graphene flake saturable absorber

Jaspreet Kaur Nagi and Soumendu Jana ^{*}

School of Physics and Materials Science, Thapar Institute of Engineering and Technology, Patiala - 147004, Punjab, India



(Received 9 August 2020; revised 12 April 2021; accepted 28 June 2021; published 12 August 2021)

Exploiting the broadband operating frequency regimes of a graphene flake saturable absorber (GFSA), a cavity soliton (CS) is excited in heretofore unexplored ultraviolet and visible regions. A broad-area device, namely, a vertical cavity surface emitting laser (VCSEL) is taken as a host of CSs; a two-dimensional (2D) transverse soliton, which is quite different from the conventional propagating one. The VCSEL with an embedded 2D homogeneous transverse layer of a GFSA is coupled with a frequency selective feedback. A CS is also generated in the infrared region, especially at the optical communication wavelength. Spontaneous dynamics and interaction behavior of CSs as well as generation of CS molecules and the push-broom effect are reported in this broad cross-sectional device. In comparison with other existing and potential models, the proposed VCSEL with GFSA model shows greater efficiency.

DOI: [10.1103/PhysRevE.104.024209](https://doi.org/10.1103/PhysRevE.104.024209)

I. INTRODUCTION

Self localized structures in extended systems have always been at the center of interest in various disciplines of science; so in nonlinear optics. In this context the cavity soliton (CS), a special type of localized confinement of light in a driven semiconductor microresonator cavity, is attracting great research interest owing to its potential as all-optical future “bits” and editable memory [1–3]. Recent investigations suggest that it may be used to realize an all-optical on-chip microscope and parallel processing of information—a major shove in current and coming days’ photonics [4,5]. CSs appear as an arrangement of bright (dark) spots sitting or moving, depending on the system parameters, on a dark (bright) homogeneous background [6]. However, a dissipative soliton inside a cavity can qualify to be designated as a CS only if it can show three basic features; plasticity (freedom of formation at any point in the transverse cavity plane), bistability (being “on” and “off” at the same cavity conditions), and exponential localization [7]. Of the various semiconductor microcavities, the vertical cavity surface emitting laser (VCSEL) is the most appreciated for excitation of CSs. The wide cross-sectional area (250 μm) and stability against temperature fluctuation made the VCSEL a unique device. Due to the small active region (typically 10 μm in diameter), VCSEL consumes 5–10 times lesser power than its edge-emitter analog [8]. VCSELs can be produced with one or two-dimensional (2D) arrays with extremely small cavity length (nearly 100 times shorter than edge emitter lasers) [9]. In addition, VCSEL architecture provides excellent coupling with single-mode and multimode fibers [8,10]. In the early years, a holding beam was used to generate homogeneous background as well as to neutralize system losses and writing pulses to excite the CS [1]. Although the theoretical prediction of CS has been done and the

precursor of it has been reported, clear experimental observations of CS have yet to be realized. This was believed to be due the hindrance of the boundary dependency of the localized pattern that should be ideally self-confined. Finally, CSs were experimentally observed by Barland *et al.* in 2002 [11,12]. However, this experimental setup uses a holding beam that can be removed to make the system much simpler by the use of a saturable absorber [1]. The CSs obtained persisted throughout the investigation (greater than one minute) and were later erased by using same pulse with opposite phase. With the holding beam, the cavity dynamics become unnecessarily complex. Later on, different VCSEL models, viz., VCSELs with saturable absorber (VCSEL-SA) [13] and VCSELs with frequency-selective feedback (VCSEL-FSF) [14] successfully removed the holding beam. The VCSEL-SA model provides bistability (a mandate for CS generation) but at the cost of increasing losses. In the recent past, we generated CSs in a VCSEL by using a combined configuration which employs saturable absorber as well as FSF to neutralize each other’s drawbacks [15].

Until a decade before, semiconductor-based saturable absorbers (SESAMs) were typical for saturable absorption in VCSELs. Although SESAMs offer a high ratio of saturable to nonsaturable loss [16], they show narrow bandwidth operation with complex fabrication and packaging procedures. It is mostly employed for Q switching and mode locking of ultrafast low-loss lasers [17,18]. Gradually, the monopoly of semiconductor-based saturable absorbers began to diminish due to the large recovery time (nearly a few hundred fs) and narrowband absorption of SESAM owing to its characteristic energy band gap [16]. These days, SESAMs are gradually being replaced by other nonlinear saturable absorbers and various 2D materials such as graphene, graphene oxide, graphene flakes, carbon nanotubes, topological insulators, black phosphorus, transitional metallic dichalcogenides, and many more [19–21]. Graphene is otherwise a widely studied material due to its optical, electrical, and mechanical properties [22–24].

^{*}soumendu.jana@thapar.edu

The planar 2D arrangement of sp^2 -hybridized carbon atoms of graphene are attached with σ bonds; which accounts for its extraordinary mechanical strength. The π bond leads to electrical and optical properties. By virtue of graphene’s characteristic conical, gapless (but not overlapping) energy band structure (with unoccupied valence band and fully filled conduction band crossing linearly at the Dirac points), electronic transitions can be expected at any frequency, in principle. The ultrashort laser pulse thermalizes a large concentration of the charge carriers, which hinders further absorption of electrons on account of Pauli blocking (a single quantum state can be occupied by only two fermions simultaneously). Thus, the absorption of light decreases and eventually saturates with increase in intensity. Saturation of absorption in graphene was first demonstrated in 2009 by using graphene as a mode-locking component. The number of layers of graphene greatly decides its optical property (single layer absorbs only 2.3% of incident light). Due to the zero band gap structure, graphene is widely used in wavelength-independent nonlinear optical devices. Nonetheless, a band gap can be artificially generated in graphene via electrostatic gating or chemical doping. It is now experimentally established that graphene and its derivatives offers excellent saturable absorption properties with low saturation strength and fast recovery time [16,25,26]. Also, use of graphene in mode locking and Q switching of various devices is increasing [27,28]. It provides wavelength-independent saturable absorption with large charge-carrier concentrations, low dissipation rate, and high mobility [25,26,29,30]. Some devices also use micron-scale suspension of graphene flakes dispersed in polymers such as polymethyl methacrylate (PMMA) as saturable absorber (SA). A dispersion of R6G (rhodamine 6G) dye and nanofabricated undoped graphene flakes in PMMA solution give rise to self-organization of light when illuminated with an initial intense pulse [31]. The pattern thus formed can be controlled and manipulated by external pumping. The output beam so obtained may vary from a few to several hundred microns in size [31,32]. A single layer of graphene exhibits about 2.3% nonsaturable loss per pass. This loss can be controlled or eliminated by using a layer of SiO_2 with varying thickness between a distributed Bragg reflector and SA layer [33]. A similar technique can be potentially used to capture losses in graphene flakes (13% per pass). Graphene flake saturable absorber (GFSA) mirrors successfully demonstrated mode locking of a laser at 190 fs pulse duration [34]. The absorption coefficient of GFSA is given as $\alpha = \alpha_0/\sqrt{1 + I/I_s} + \alpha_{ns}$, where I is the intensity of the given radiation, α_0 is the low-intensity absorption coefficient, I_s is the saturation intensity, and α_{ns} is the nonsaturable absorption coefficient [31]. To the best of our knowledge, GFSA has not been used as saturable absorber in VCSEL. However, the replacement of SESAM by a GFSA layer looks lucrative in view of its broadband operational wavelength range. In this work we use GFSA as (1) the only active layer, (2) the only passive layer, and (3) both the active and passive layers (which henceforth will be referred to as an active-passive layer) of saturable absorber in the VCSEL, which is coupled with frequency-selective feedback (FSF) to generate CSs in different regions of EM spectra. Furthermore, we discuss the comparative study of VCSEL embedded with different saturable absorbers such as

SESAM, graphene, and graphene flakes. Also, we discuss a unique configuration of VCSELs which leads to a more energy efficient model.

II. MATHEMATICAL MODELING

The bistability, a prerequisite for the formation of CS has been achieved in two popular ways in previous models. Some models couple a FSF with VCSEL (VCSEL-FSF model) to achieve “dispersive bistability” (please see Refs. [5,35] for the Littrow configuration and also Refs. [36–38] for FSF). Alternatively, some CS models use a SA in VCSEL (i.e., VCSEL-SA model) to achieve absorptive bistability [13,39,40]. Our present VCSEL-FSF-SA model of the CS laser (a schematic diagram is given in Fig. 1) includes both SA in VCSEL and couples the FSF in order to achieve the desired bistability of the CS hosting system as well as to compensate for the loss. The delay in feedback is negligible.

The governing equation describing the cavity dynamics using graphene flake saturable absorber as active, passive, and active-passive medium and coupled with frequency-selective feedback can be written in form of coupled rate equations as follows [13,15,41]:

$$\frac{\partial E}{\partial t} = [-(1 - i\theta) + (1 - i\alpha)d_a + (1 - i\beta)d_p + \alpha_{ns} + i\Delta]E + F, \tag{1}$$

$$\frac{\partial d_a}{\partial t} = -c_a[d_a\sqrt{1 + g_1|E|^2} - \mu], \tag{2}$$

$$\frac{\partial d_p}{\partial t} = -c_p[d_p\sqrt{1 + sg_2|E|^2} + \gamma], \tag{3}$$

$$\frac{\partial F}{\partial t} = -(\lambda + i\Omega_0)F + \sigma\lambda E. \tag{4}$$

Here, E is the slowly varying cavity field amplitude and F is the feedback field.

The feedback is given by a volume Bragg grating (VBG) and the delay in feedback is negligible. The VBG has a Lorentzian frequency response and the central frequency is considered as the reference frequency [37]. Thus, the VBG, which is a reflector with frequency filter, acts as a frequency-selective feedback (FSF). The FSF lowers the laser threshold value in a very narrow frequency region around the peak of the Bragg reflection [14]. The feedback becomes negligible if one goes far from the frequency zone [42]. Also, the eigenvalue

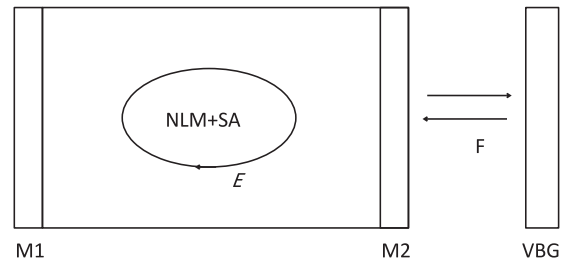


FIG. 1. Schematic of a cavity soliton laser with saturable absorber and frequency-selective feedback. $M1$, $M2$ are the mirrors. VBG is the volume Bragg grating, NLM and SA stand for nonlinear media and saturable absorber, respectively.

separation method given in Ref. [41] may reveal that the presence of FSF leads to the soliton solutions of the governing equation. In the rate equations the time t is scaled to cavity round trip time. θ , the cavity mistuning, measures the detuning between driving field and cavity. The parameters α and β are the linewidth enhancement factor for active and passive medium, respectively, and quantify the coupling strength of amplitude and phase. The variables d_a and d_p are carrier densities for active and passive media, respectively. The amount of absorption which cannot be saturated is represented by α_{ns} . c_a (c_p) and μ (γ) represent the ratio of carrier-to-photon lifetime and pump parameter, respectively, for active (passive) media. The parameter s is the saturation strength. The variable g_1 and g_2 represent the saturable absorption of the graphene flakes for an active and passive media, respectively. The parameters λ , Ω_0 , and σ signify the bandwidth, resonance frequency, and feedback strength (coupling strength) of the feedback field, respectively.

CSs can be excited in the homogeneous cavity by using an injected pulse. The trivial homogeneous steady-state (HSS) solution of the system [Eqs. (1)–(4)] can be determined as

$$E = 0, \quad F = 0, \quad d_a = \mu, \quad d_p = -\gamma, \quad (5)$$

whereas the nontrivial HSS is

$$E = \sqrt{I} \exp^{iqx - (\omega + q^2)t}, \quad (6)$$

$$d_a = \frac{\mu}{\sqrt{1 + g_1 I}}, \quad (7)$$

$$d_p = \frac{-\gamma}{\sqrt{1 + sg_2 I}}, \quad (8)$$

$$F = \frac{\sigma \lambda E}{\lambda + i\Omega_0}. \quad (9)$$

Here, q is the transverse wave vector and $I = |E|^2$. Thus the solution given by equation (6) represents a tilted traveling wave. In a homogeneous steady state the wave vector can be considered as $q = 0$ due to the absence of the wave-vector selection mechanism. So, the HSS solution becomes $E = \sqrt{I} \exp^{-i\omega t}$. Equations (7)–(9) have been derived by using the steady-state conditions $\frac{\partial d_a}{\partial t} = 0$, $\frac{\partial d_p}{\partial t} = 0$, and $\frac{\partial F}{\partial t} = 0$, respectively. Putting the nontrivial HSS given by Eqs. (7)–(9) into Eq. (1), we get the cavity field equation in the form of the modified complex Ginzburg-Landau equation (CGLE) as follows:

$$\frac{\partial E}{\partial t} = \left[-(1 - i\theta) + \frac{\mu(1 - i\alpha)}{\sqrt{1 + g_1 I}} - \frac{\gamma(1 - i\beta)}{\sqrt{1 + sg_2 I}} + \alpha_{ns} + i\Delta \right] E + (a - ib)E, \quad (10)$$

where $a = \frac{\sigma \lambda^2}{\lambda^2 + \Omega_0^2}$, $b = \frac{\sigma \lambda \Omega_0}{\lambda^2 + \Omega_0^2}$, and I is the instantaneous intensity. However, a more generic and physically delicate procedure to derive the modified CGLE [i.e., Eq. (10)] from Eqs. (1)–(4) has been given in Ref. [43]. A recent treatment of the CGLE for fast media was proposed in Ref. [44]. A variety of modified CGLE-class models has been widely used in different contexts, e.g., exact solutions [45], stable stationary solitons [46], pattern selection and modulation instability [47], and temporal solitons [48]. Equation (9) indicates that, in the state-steady condition, the fields E and F are linearly coupled. It may be mentioned here that coupling of the cavity

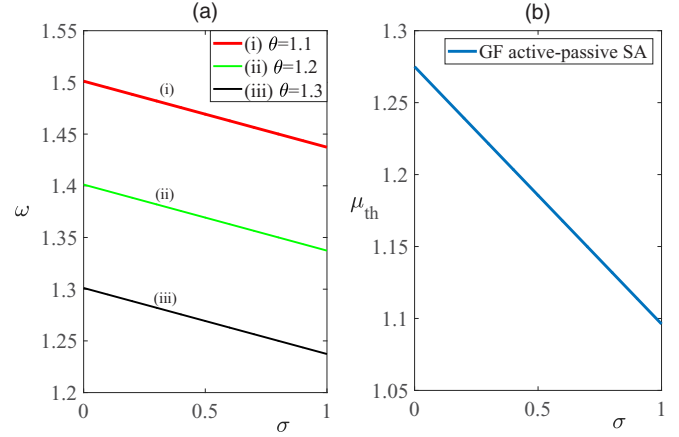


FIG. 2. (a) Variation of reference frequency ω with feedback σ at $I = 1$ and $g_2 = 2$. (b) Variation of threshold pump parameter μ_{th} with σ . Here and further, $\alpha = 2.5$, $\gamma = 0.3$, $\beta = 0$, $s = 10$, $\Omega_0 = 1.5$, $\lambda = 0.7$, and $\alpha_{ns} = 0.025$.

to a resonant linear system (here feedback) may lead to the stabilization of the solution of even the cubic Ginzburg-Landau equation, which generally has no stable solution [41].

The real part of Eq. (10) reveals the relation for I as

$$\frac{\mu}{\sqrt{1 + g_1 I}} = 1 - a + \frac{\gamma}{\sqrt{1 + sg_2 I}} - \alpha_{ns}. \quad (11)$$

The imaginary terms of Eq. (10) yield the reference frequency as

$$\omega = -\theta + b + (1 - a)\alpha + \frac{\gamma(\alpha - \beta)}{\sqrt{1 + sg_2 I}} - \alpha_{ns}\alpha. \quad (12)$$

According to Eq. (12), the reference frequency ω varies with field intensity and the saturation parameter of the GFSA provided that the active layer has a different linewidth enhancement factor from the passive layer (i.e., $\alpha \neq \beta$). Also, ω depends on the GFSA if used as a passive layer. It is invariant if the active layer is a GSA or a GFSA, or a SESAM. The nonsaturable absorption parameter of GFSA also aids in reducing the reference frequency. Apart from these the reference frequency ω is also reliant on frequency-selective feedback components (λ , σ , and Ω) and cavity detuning θ . Reference frequency ω decreases linearly with a slope of 0.064 as the feedback strength σ of the FSF increases [Fig. 2(a)]. For a given σ value, ω decreases with increasing detuning parameter θ . Although we investigated CSs for a range of parameters, we choose a typical set of values as the system parameters: $\alpha = 2.5$, $\theta = 1.1$, $\mu = 1.15$, $\gamma = 0.3$, $\sigma = 0.6$, $\beta = 0$, $s = 10$, $\Omega_0 = 1.5$, $\lambda = 0.7$, and $\alpha_{ns} = 0.025$ to present our results. All the figures are plotted with these values unless mentioned otherwise.

We now determine the pump threshold of laser by putting $I = 0$ in Eq. 11 as

$$\mu_{th} = 1 - a + \gamma - \alpha_{ns}. \quad (13)$$

The quantity μ_{th} decreases linearly with a slope of 0.18 as σ increases [Fig. 2(b)]. The trivial HSS remains stable only in the region where $\mu < \mu_{th}$. Before discussing the stability of the nontrivial HSS the limit of the saturation parameter at

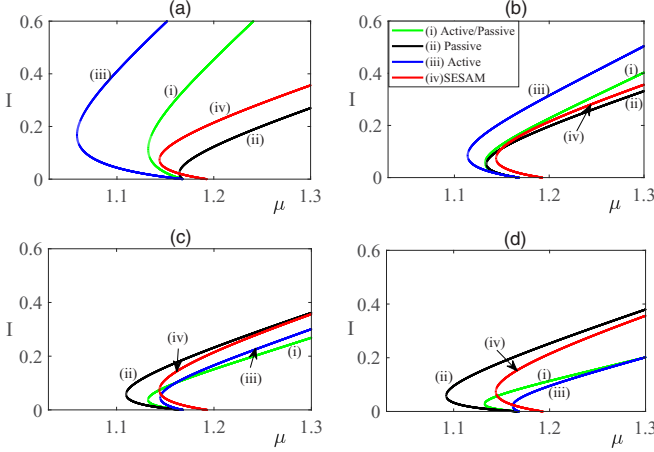


FIG. 3. Variation of CS intensity I with pump parameter μ for GFSAs as active layer, passive layer, and both active and passive layers. For comparison, each panel contains a variation curve for SESAM (active-passive both layers). The four panels are plotted for different strengths of GFSAs (considering $g_1 = g_2 = g$) as (a) $g = 1$, (b) $g = 2$, (c) $g = 3$, and (d) $g = 4$. Here, $\sigma = 0.6$ while rest of the parameters are same as in Fig. 2. The legends in panel (b) are valid for all the plots (a)–(d).

laser threshold condition [i.e., Eq. (13)] can be determined as

$$s > \frac{2g_1}{g_2} \left(\frac{1 - a - \alpha_{ns}}{2\gamma - (1 - a - \alpha_{ns})(3g_1I)} \right). \quad (14)$$

It can be noted that a nonlinear, dissipative, spatially extended system, like our present model, supports pattern formation. To be more precise, the dissipation leads to intriguing spatiotemporal pattern formation in systems which are driven away from equilibrium by diffusion [49]. Moreover the feedback makes it more versatile. The spontaneous breaking of spatial symmetry in such “far-from-equilibrium system” leads to either extended patterns (e.g., hexagons, rolls) or localized patterns (e.g., vortices, fronts, spatial solitons) [1,50]. CSs can be considered as a localized patterned state placed over a stable unpatterned background state. This can be clarified by using a “homoclinic snaking” diagram [1]. Theoretically, the patterned state and CS exist below the subcritical modulation instability threshold. Experimentally, by increasing the value of the system control parameters (e.g., pump energy, feedback) the pattern can appear at the threshold of modulation instability. Thereafter, it may grow smoothly or jump to a large-amplitude state. Now, if the control parameter is reduced, the pattern can be preserved until a saddle-node bifurcation point appears, wherein the patterned state decays to an unpatterned state. Thus, for a subcritical case both the patterned and unpatterned states coexist in the same spatial domain. This bistability is essential for spatial dissipative solitons and CSs. Now, a localized structure called a “front” is generated at their boundary. In two dimensions such a front leads to CS formation.

Figure 3 shows the variation of CS intensity I with pump power μ for graphene flakes (GFSAs) as active, passive, and active-passive saturable absorber. In this communication, when the GFSAs are used as only the active layer (only the passive layer), the other layer, i.e., the passive (active) layer,

is a SESAM, unless mentioned otherwise. Notably, under the condition stated in Eq. (11), the plots of nontrivial HSS appear partly parabolic, as shown in Fig. 3. For a given value of μ the intensity can have two values from two arms of the parabolic curve, which corresponds to two CSs, i.e., bistable CS can be generated. The origin of the bistability of CS depends on graphene flakes active as well as passive saturable absorption and various other system parameters. However, the nature of stability corresponding to each arm of the parabolic curve may be different. In fact, numerical analysis reveals that the negative slope branch corresponds to unstable CSs, while the positive slope branch is partly stable and partly unstable. However, the bistability can be observed for a short range of pumping, for example, in Fig. 3(a) the range of bistability (i.e., $\mu_{th} - \mu_{tp}$) is 0.106, 0.002, and 0.034 for the active, passive, and active-passive configuration, respectively. Thereafter, only a single stability line is observed and bistability disappears.

The turning points and the corresponding intensities at the turning point of the parabolas can be determined for the GFSAs as active, passive, and active-passive media as follows:

$$\mu_{tpa} = \sqrt{1 + g_1 I_a} \left(x + \frac{\gamma}{1 + s I_a} \right), \quad (15)$$

where

$$I_a = \frac{-2xg_1 + g_1\gamma + \sqrt{g_1^2\gamma^2 + 8xg_1\gamma(s + g_1)}}{2xg_1s}, \quad (16)$$

$$\mu_{tpp} = (1 + I_p) \left(x + \frac{\gamma}{\sqrt{1 + sg_2 I_p}} \right), \quad (17)$$

where

$$I_p = \frac{\gamma(sg_2 - 2) - 2x}{3xsg_2 + \gamma sg_2}, \quad (18)$$

and

$$\mu_{tpb} = \sqrt{(1 + g_1 I_b)} \left(x + \frac{\gamma}{\sqrt{1 + sg_2 I_b}} \right), \quad (19)$$

where

$$I_b = \frac{1}{sg_2} \left[\left(\frac{\gamma(sg_2 - g_1)}{xg_1} \right)^{\frac{2}{3}} - 1 \right]. \quad (20)$$

Here, $x = 1 - a - \alpha_{ns}$.

In Eqs. (15)–(20), μ_{tpa} , μ_{tpp} , and μ_{tpb} represent the pump parameters of active, passive, and active-passive media, respectively. I_a , I_p , and I_b are the corresponding intensities at the onset of bistability. Figure 3(a) shows that, for lower saturable absorption, less pumping energy is required when using graphene flakes as active saturable absorber in VCSEL. Among the already mentioned three configurations of VCSEL, passive SA requires the greatest amount of pump energy. As we increase saturable absorption of graphene flakes simultaneously for active and passive SA, the range between lowest and the highest value of pumping decreases [cf. Figs. 3(a) and 3(b)]. Further increasing the saturable absorption of graphene flakes leads to switching between the nature of the curves, i.e., passive SA requires the least pumping energy, whereas active SA requires the most and active-passive SA requires an intermediate amount [Figs. 3(c) and 3(d)]. The turning

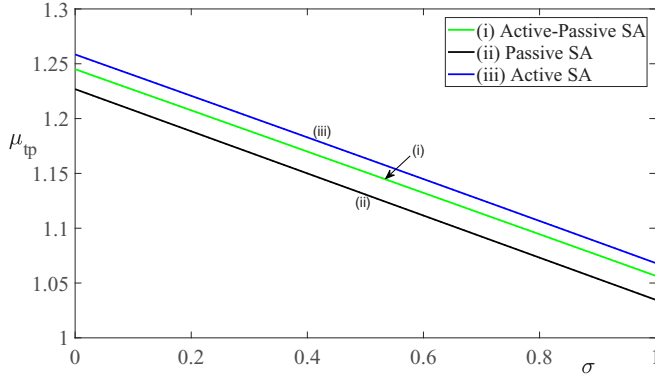


FIG. 4. Variation of turning point μ_{tp} with feedback strength σ for GFSA as (only) active layer, (only) passive layer, and both active and passive layers. Here $g_1 = g_2 = 3$ while the rest of the parameters are the same as in Fig. 2.

point μ_{tp} falls linearly with slope 0.19 as feedback strength σ increases (Fig. 4).

III. COMPARISON OF DIFFERENT MODELS OF VERTICAL CAVITY SURFACE EMITTING LASER

So far we have discussed the generation and dynamics of CSs in VCSELs embedded with graphene flake saturable absorbers coupled with FSF. Until the advent of graphene and graphene-based saturable absorbers, ultrafast lasers were basically reliant on semiconductor-based saturable absorbers. Recently we proposed successful generation of CS in VCSEL using graphene as saturable absorber. The broadband absorption of graphene and graphene flakes made it possible to excite CS in ultraviolet as well as visible region. Here, we compare the different VCSEL models, namely, VCSEL with semiconductor SA (VCSEL-SESAM-FSF), VCSEL with graphene SA (VCSEL-GSA-FSF) and VCSEL with graphene flakes SA (VCSEL-GFSA-FSF). FSF is provided in all of them to compensate cavity losses. The variation in intensity of CSs with pump parameter is shown in Fig. 5. The

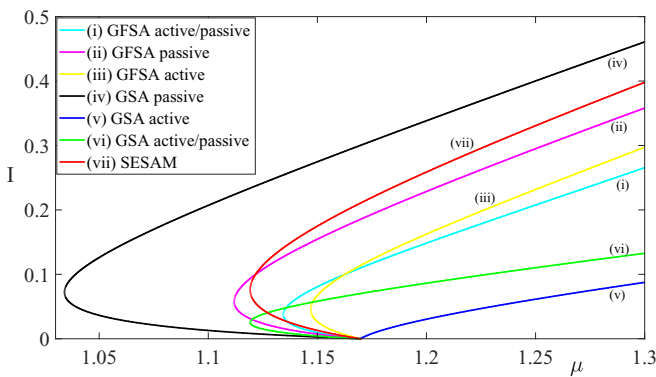


FIG. 5. Variation of CS peak intensity I with μ for different saturable absorbers in a VCSEL. When only one layer between the active and passive layers is GFSA or GSA the other layer is SESAM. The turning points μ_{tp} are remarkably different in different media. Here $\sigma = 0.6$ and $g_1 = g_2 = 3$, while the rest of the system parameters are the same as in Fig. 2.

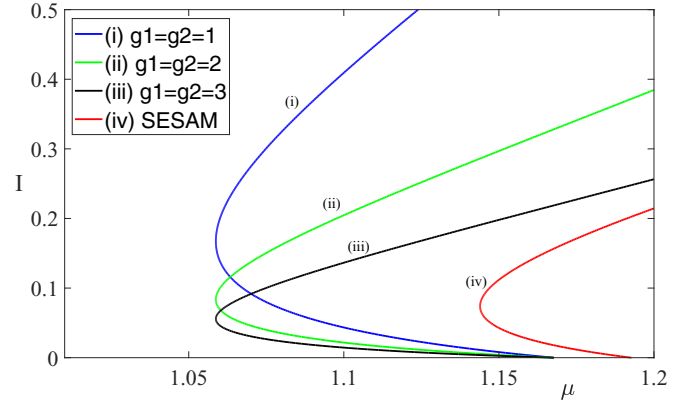


FIG. 6. Variation of CS peak intensity I with μ in VCSEL using GFSA as an active layer as well as GSA as a passive layer. Also, the variation for the case of SESAM in both layers is plotted for comparison. Here $\sigma = 0.6$, where the rest of the parameters are the same as in Fig. 2.

turning point as well as range of pump power vary remarkably for different VCSEL models. The value of all graphene and graphene-based saturation parameter is kept the same ($g_1 = g_2 = 3$). From Fig. 5 it can be comprehended that, for given set of parameters out of three models, the performance of VCSEL-GSA is comparatively better because it requires the least pump power to generate CSs. For passive and active-passive configurations, graphene shows the least requirement for pump power than its corresponding graphene flakes counterpart. While graphene active SA requires more pump power in all configurations in our case, the pump power of semiconductor SA-based VCSEL lies in between. Except for graphene-active SA, CSs show a bistable nature in all configurations of VCSEL. Table I compares various system parameters such as ω , s , μ_{th} , μ_{tp} , and $|\mu_{th} - \mu_{tp}|$ for VCSEL-SESAM-FSF, VCSEL-GSA-FSF, VCSEL-GFSA-FSF, and VCSEL-GFSA-GSA-FSF models using $g_1 = g_2 = 2$. Here, graphene passive saturable and graphene flakes active SA need the least pumping (μ_{tp}) of all layouts of graphene and graphene flake SA, respectively. This leads to a comparatively efficient configuration of VCSEL, viz., VCSEL-GFSA-GSA-FSF. In this model, GFSA serves as active SA and GSA as passive SA. For a given set of parameters ($\sigma = 0.6$, $\gamma = 0.3$, $\beta = 0$, $s = 10$, $\Omega_0 = 1.5$, $\lambda = 0.7$, and $\alpha_{ns} = 0.025$), VCSEL-GFSA-GSA-FSF yields CSs only for a particular range of $g_1 (=g_2) = 1.1-2.3$. Also for this configuration, the turning point intensity decreases with increasing g_1 and g_2 simultaneously (Fig. 6). Table I can be used for experimental verification of CS(s) in VCSEL. Figure 7 portrays that this combined model is 11.6%, 12.8%, and 13.7% more power efficient than the VCSEL-GSA-FSF, VCSEL-GFSA-FSF, and VCSEL-SESAM-FSF model, respectively. In the sections we explore the formation of CS in various regions of EM spectra. Now we generate CSs with a different SA model corresponding to Fig. 8. For all cases multiple CSs of nearly similar peak intensity are formed [Figs. 8(a)–8(d)]. For a better visualization of the profile one peak each from Figs. 8(a)–8(d) are taken and plotted in Fig. 8(e). Equation (10) may also give rise to a single CS solution. To find the number of CSs for a given

TABLE I. Comparison of ω , s , μ_{th} , μ_{tp} and range of stable CS ($|\mu_{th} - \mu_{tp}|$) for different VCSEL models.

Microresonator model	ω	s	μ_{th}	μ_{tp}	Range of stable CS
VCSEL-SESAM-FSF	2.1117	3.9757	1.1927	1.1439	0.0488
VCSEL-GSA-FSF (active)	2.0992	7.9180	1.1677	1.1623	0.0054
VCSEL-GSA-FSF (passive)	2.0992	1.9795	1.1677	1.0617	0.1060
VCSEL-GSA-FSF (both)	2.0992	3.9590	1.1677	1.1171	0.0506
VCSEL-GFSA-FSF (active)	2.0992	2.9590	1.1677	1.1140	0.0537
VCSEL-GFSA-FSF (passive)	2.0992	1.0377	1.1677	1.1345	0.0332
VCSEL-GFSA-FSF (both)	2.0992	3.9590	1.1677	1.1323	0.0354

set of parameters, we plot the feedback field with respect to the CS intensity (Fig. 9) under steady-state conditions. Depending on the parameters, a unique solution [Fig. 9(a)] or a multiple solution [Fig. 9(b)] can be achieved. Table II lists the parametric range for unique and multiple CS solutions.

Graphene’s optical response and absorption of electromagnetic radiation are different in different spectral regions (as it is decided by its unique band structure, zero band gap, and the interaction of the Dirac fermions with the electromagnetic radiation). For example, a radiation from visible to near-infrared causes intraband transitions, while the far-infrared absorption occurs through either intraband transitions or free carrier absorption.

At this point the localization of CS structure via modulation instability (MI) is in order. The interplay between the nonlinearity and diffraction (for spatial domain) initiates MI of the steady-state solution; which in turn leads to the pattern formation [51]. Being a spatially extended, highly nonlinear system, the present model too possesses a pattern-forming MI. The trivial HSS is stable if $\mu < \mu_{th}$. Similar to Fig. 3, in Figs. 5–7 the negative slope (i.e., the lower) branches of the C-shaped curves are unstable, while the major parts of the positive slope (i.e., upper) branches are stable. The rest of the upper branch may show Hopf instability (a type of dynamical instability that gives birth to a limit cycle) for μ values less than the threshold of the Hopf instability (μ_H). μ_H can be tuned by choosing suitable values of γ , s , g_2 and, importantly, the ratios of photon lifetime to carrier lifetime for both active

and passive media. The upper branches also show MI against spatially modulated perturbation (diffraction induced). This is called a Turing instability. The CSs presented in this paper correspond to the Turing unstable and Hopf stable part of the upper branches of the curves (of Figs. 3, 5, and 6). Initially, a nonlasing state and MI-induced filamentation is obtained. By adjusting the carrier density decay rates it is possible to localize the CS.

IV. ULTRAVIOLET REGION

In this and subsequent sections we use GFSA in three different configurations, i.e., active medium, passive medium, and active-passive media. When the GFSA is used as an active or passive medium, the other layer is considered as SESAM. Graphene flakes exhibit broadband absorption owing to the gapless energy band structure of graphene. CSs are mostly generated in the infrared region. Here, we put to use the broadband proficiency of graphene flakes to generate CSs in different regions of the electromagnetic spectra such as the ultraviolet region, the visible region, and the infrared region, especially at the optical communication wavelength.

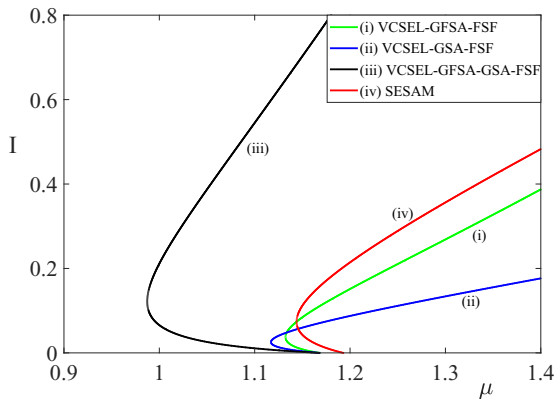


FIG. 7. Variation of CS peak intensity I with μ in VCSEL using GFSA as active-passive both layers, GSA as active-passive both layers, GFSA active and GSA passive layers, and SESAM as both layers. Here $\sigma = 0.6$ and $g_1 = g_2 = 3$, and the rest of the parameters are the same as in Fig. 2.

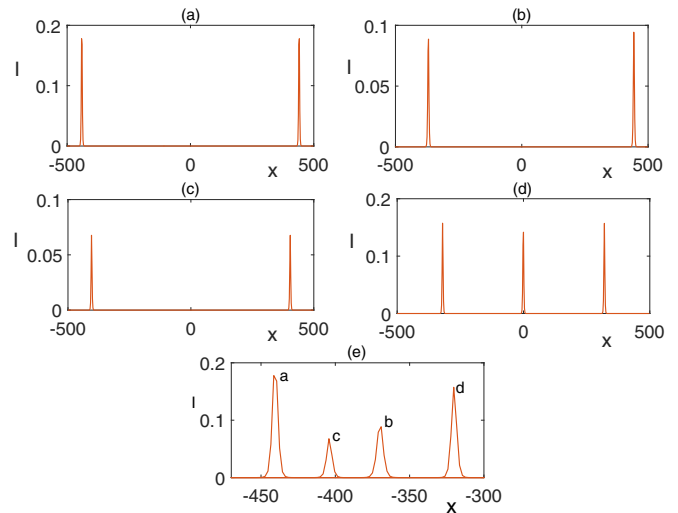


FIG. 8. CS profile corresponding to different VCSEL models described in Fig. 7. (a) VCSEL-SESAM-FSF with $\mu = 1.16$. (b) VCSEL-GFSA-FSF with $\mu = 1.14$. (c) VCSEL-GSA-FSF with $\mu = 1.131$. (d) VCSEL-GFSA-GSA-FSF with $\mu = 1.079$. For an enlarged view of the CS profile, one CS from each panel (a)–(d) is taken and replotted in panel (e). For panels (a)–(e), $\theta = 1.1$, and rest of the parameters are the same as in Fig. 7.

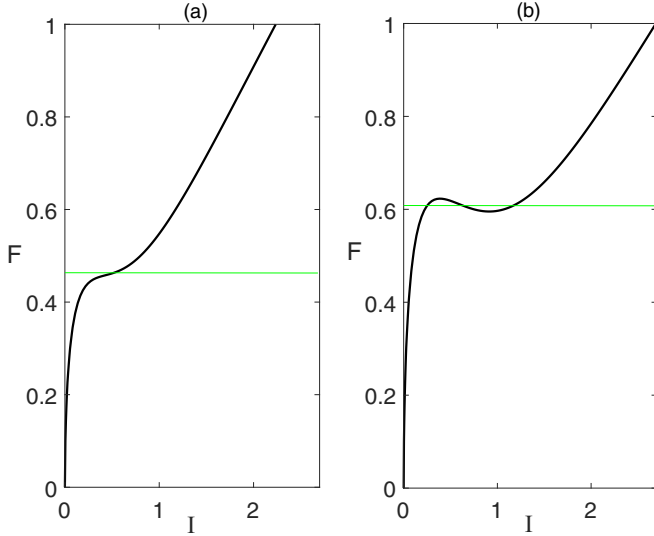


FIG. 9. Plot of feedback F as a function of intensity I . (a) Unique solution with $\mu = 1.02$ and (b) multiple solution with $\mu = 1.22$. Here $\theta = 1.1$ while the rest of the parameters are the same as in Fig. 2.

For this we numerically solve the governing modified CGLE [Eq. (10)] by using the split-step Fourier method to generate bright CSs. The choice of the initial ansatz is crucial for the success of the numerical solution. A cubic Ginzburg-Landau equation can have an exact solution but is unstable [52]. Introduction of quintic nonlinearity may lead to the stabilization of the solution. Since the saturable nonlinearity can be approximated as a cubic-quintic nonlinearity, our current model possesses a stable solution. Now the semiconductor laser cavity dynamics with feedback can be studied following two different models: one that considers the carrier dynamics (referred to as the “class B model”) and the other that does not (referred to as the “class A model”) [53]. Previously, we reduced Eqs. (1)–(4) to Eq. (10) (i.e., from the class B model to the class A model). The solution of such a class A model with zero detuning can be determined by the chirped-sech ansatz of form [41,53,54] $E(x, t) = E_{\max}[\cosh(Kx)]^{-1-i\beta} e^{i\omega t}$. Although our model has nonzero detuning, we consider the chirped-sech ansatz as the initial ansatz for our numerical computation. The method of finding the exact stable solution for an asymmetric linearly coupled Ginzburg-Landau equation has been developed [53,54]. Also, two linearly

TABLE II. Parametric variables for single solution and multiple solutions.

Parameter	Unique solution	Multiple solutions
θ	≤ 0.96	> 0.96
μ	≤ 1.09	> 1.09
γ	≥ 0.55	< 0.55
α	≤ 1.91	> 1.91
g_1	≤ 0.8	> 0.8
g_2	≤ 0.86	> 0.86
s	≤ 2.8	> 2.8

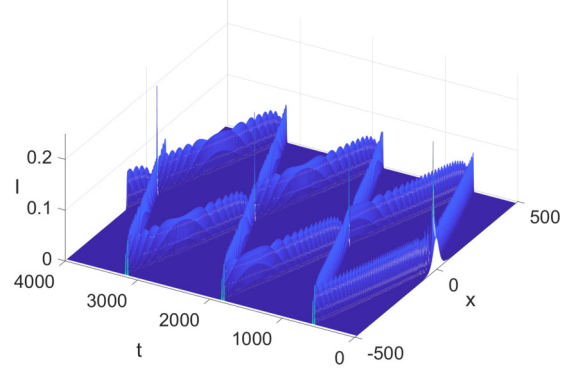


FIG. 10. Evolution of CSs in the ultraviolet region using GFSA as active-passive layer. Here, $\alpha = 2.5$, $\theta = 1.1$, $\mu = 1.15$, $\gamma = 0.3$, $\beta = 0$, $s = 10$, $\Omega_0 = 1.5$, $\lambda = 0.7$, $g_1 = g_2 = 3$, $\sigma = 0.55$, and $\alpha_{ns} = 0.025$.

coupled complex Ginzburg-Landau equations (one with gain as well as dissipation and the other with only dissipation) may have a stable soliton solution [55]. Similarly, a stable soliton solution can be achieved with two linearly coupled nonlinear Schrödinger equations; one with loss and the other with gain [56].

As mentioned earlier we choose the system parameters the same as in Fig. 2, unless mentioned otherwise. Generally, when the writing beam is injected in the microcavity, it goes through an initial energy-balancing dynamics and emerges as a single CS or a cluster of CSs once the twofold balance (self-diffraction self-focusing and cavity loss external gain) is achieved. In the current model we always observe fragmentation of the writing beam into two or more CSs. A typical profile of CS generation and dynamics, where the writing beam eventually creates two periodically colliding CSs, is described in Fig. 10. All the CSs and CS clusters using this model involve spontaneous drift and/or collision. To visualize the CS path and collision dynamics henceforth we plot their evolution in the form of contour plots. Since the CS width is very small (≈ 20 in normalized units) with respect to the transverse dimension x of the cavity (-500 to 500), the contour plots of the CS appear as lines. So those lines can be considered as the trajectories of the cavity solitons. Moreover, in some figures [e.g., Fig. 11(c)] two trajectories, and in some figures [e.g., Figs. 11(a) and 11(b)] four or more trajectories appear. This is because the initial beam splits into two or more CSs very promptly and then exhibits different dynamics (mostly colliding). Also, in some figures [panels (b) and (c) of Figs. 13–16] the number of trajectories becomes one after the initial collision dynamics. This is because the initially generated multiple CSs eventually form a composite CS or CS molecule. Moreover, the numerical experiments are done with one spatial transverse dimension of the cavity; accordingly the CS trajectories to be interpreted. The generation and dynamics of CSs in VCSEL using graphene flakes as active, passive, and active-passive saturable absorber can be clearly visualized in Figs. 11(a)–11(c), respectively. The nature of interaction dynamics is significantly different in all three configurations. Also, the amount of corresponding feedback strength required to generate CS is different in all three cases.

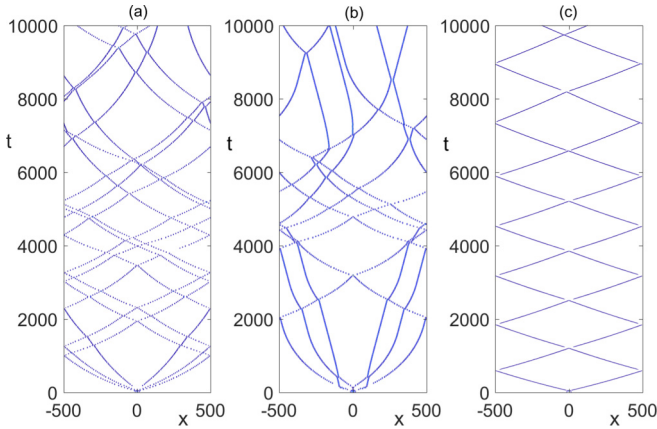


FIG. 11. Evolution of CS in ultraviolet region using GFSA as (a) active layer at $\sigma = 0.6$, (b) passive layer at $\sigma = 0.5$, and (c) active-passive layer at $\sigma = 0.55$. The rest of the parameters are kept same as in Fig. 10.

To use GFSA as active saturable absorber, we set $g_1 = 3$ and a semiconductor saturable absorber is treated as passive saturable absorber (i.e., $g_2 = 1$). When a single initial beam is injected into the cavity, it splits into multiple fragments that eventually emerges as CSs [Fig. 11(a)]. At the beginning CSs almost regularly collide and oscillate. With time, the CSs gradually shift from regular, periodic oscillations to an irregular trend. However, in case of GFSA passive medium (keeping $g_2 = 3$) and semiconductor saturable absorber as active medium, multiple CSs are generated that show rather random dynamics from the beginning [Fig. 11(b)]. A rhythmic, regular oscillation is observed using GFSA as active-passive media (using both $g_1 = g_2 = 3$) [Fig. 11(c)]. Factually, CSs are extremely sensitive to any type of inhomogeneity caused by any gradient in the system parameters such as cavity detuning, intensity, and phase. Even thermal gradient, gradient in injected beam, gradient in feedback field and the phase of feedback field can cause spontaneous drift in CSs.

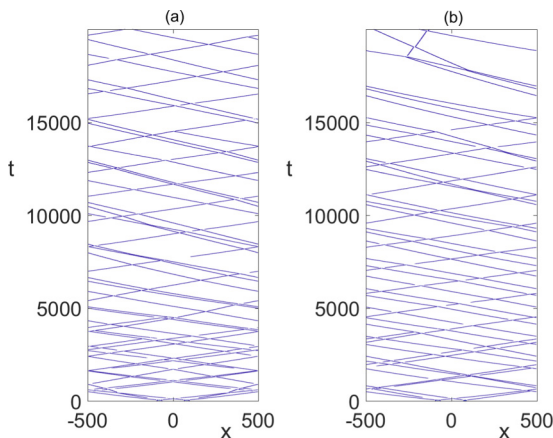


FIG. 12. Interaction of CSs of (a) same amplitude and (b) different amplitude with $\sigma = 0.55$. The rest of the parameters are the same as in Fig. 10.

Apart from spontaneous drift, the interaction dynamics need to be investigated in order to verify the fundamental behavior of solitons as well as to explore any potential novel dynamics. Such interaction behavior of CSs (Fig. 12) is significantly different from that of spontaneous drift (Fig. 11). Whether both interacting CSs are of the same amplitude [Fig. 12(a)] or different amplitude [Fig. 12(b)], the CSs collide quite regularly and periodically in the beginning. However, with time the regular trend of oscillation and collisions fades in both the cases. For beams with unequal amplitudes, eventually the two CSs combine and continue to drift [Fig. 12(b)]. The dynamics of the CS can be controlled by the inhomogeneity in the system.

V. VISIBLE REGION

So far we have discussed the generation and dynamics of CS in the UV region. Moving further we now excite CSs in the visible region of the electromagnetic spectrum. As in the UV region, here also we use GFSA as active, passive, and active-passive medium. For an active and active-passive saturable absorber, a single initial beam splits into two CSs [Figs. 13(a) and 13(c)]. A regular collision is observed in the case of active as well as active-passive SA. However, the point of collision slowly shifts with evolution for active-passive SA. In both cases, eventually the two CSs unite to form a single composite CS which propagates in the cavity. The composite CSs are sometimes termed a “CS molecule.” As already mentioned, the motion of the CS or CS molecule is guided by the inhomogeneity of the cavity. Also, CSs move faster in the beginning and then gradually the velocity of CSs decreases in both cases. The most interesting point is the opposite direction of drift of the composite CSs in these two cases. Now, for the case of GFSA as passive medium, the initial beam again splits into multiple peaks or CSs. They collide and repel each other occasionally [Fig. 13(b)]. The collisions becomes less frequent with time. Also, no velocity change is observed due to collision.

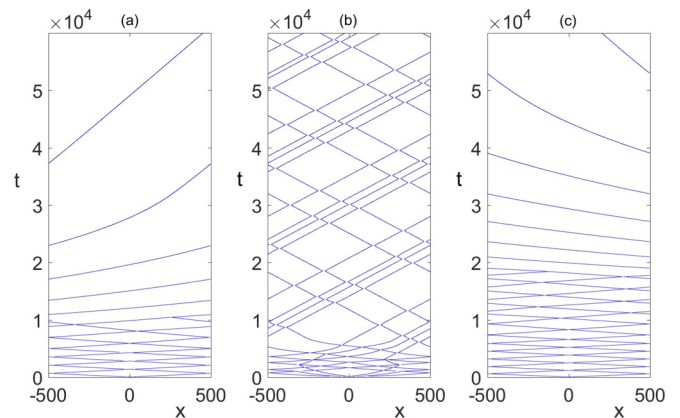


FIG. 13. Evolution of CS in visible region using GFSA as (a) active layer at $\sigma = 0.6$, (b) passive layer at $\sigma = 0.5$, and (c) active-passive layer at $\sigma = 0.55$. The rest of the parameters are kept the same as in Fig. 10.

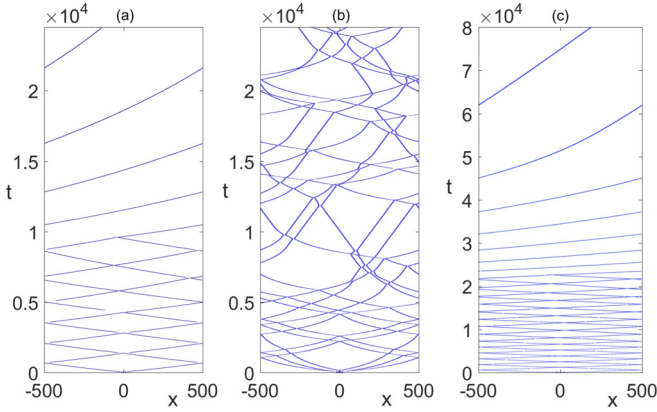


FIG. 14. Generation and dynamics of CS in the infrared region (wavelength is 980 nm) with GFSA as (a) active layer at $\sigma = 0.6$, (b) passive layer at $\sigma = 0.5$, and (c) active-passive layer at $\sigma = 0.55$. The rest of the parameters are kept the same as in Fig. 10.

VI. INFRARED REGION

The infrared region is the most familiar region for CS generation in VCSELs. The reason is that the energy band gap of commonly used semiconductor SAs falls in this region. The importance of infrared CS grows due to its numerous potential applications ranging from medical imaging to astronomical use through an optical frequency comb. Therefore, it is equally significant to generate CS in infrared region of the electromagnetic spectrum as well. We here discuss CSs and their cluster formation at 980 nm wavelength. As in previous sections, GFSA is used in three layouts, viz., active medium, passive medium, and active-passive media. As expected, CSs show variety in dynamics for different configurations. The rhythmic collision-oscillation is visualized for both active [Fig. 14(a)] and active-passive [Fig. 14(c)] GFSA. The oscillation continues for a longer period in the case of active-passive media. Thereafter, in both cases, CSs combine to form a CS molecule, which travels with varying speed [Figs. 14(a) and 14(c)]. The speed is faster for GFSA active medium as compared with active-passive GFSA. A CS molecule cannot originate in a GFSA passive medium; rather, the CSs oscillate arbitrarily [Fig. 14(b)].

VII. OPTICAL COMMUNICATION WAVELENGTH

Nowadays, VCSEL is commercially used as optical interconnects in optical fiber communication system and devices [8,9]. So, we especially discuss CS generation at telecommunication wavelengths, namely, 1330 and 1550 nm. The VCSEL-FSF system with GFSA as passive medium shows random collisions in the beginning for 1330 nm [Fig. 15(b)] as well as for 1550 nm [Fig. 16(b)]. Later the CSs collide less frequently and more systematically, but no CS molecules can be generated. For GFSA active [Figs. 15(a) and 16(a)] and active-passive media [Figs. 15(c) and 16(c)], CSs unite to form CS molecule after some initial collisions and drift thereafter. For 1330 nm, CS molecules in active GFSA medium drift in opposite directions of that in cases of the GFSA active-

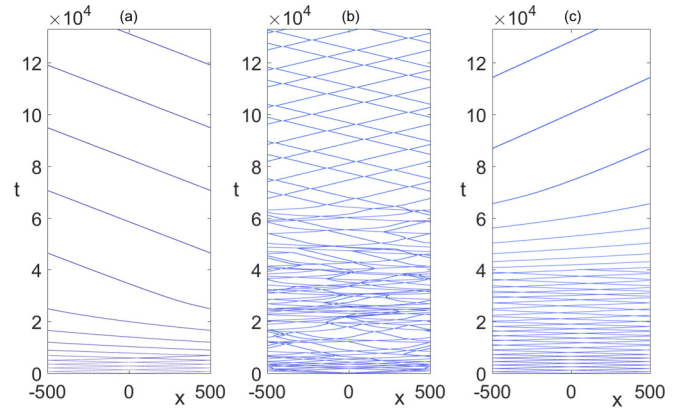


FIG. 15. Evolution of CS at the optical communication wavelength 1330 nm with a single initial pulse with GFSA as (a) active layer at $\sigma = 0.6$, (b) passive layer at $\sigma = 0.5$, and (c) active-passive layer at $\sigma = 0.55$. The rest of the parameters are kept the same as in Fig. 10.

passive medium. However, the direction of CS molecule drift is the same in both the cases for 1550 nm.

Finally, we investigate the interaction of two beams with an initial phase difference between them. Interesting interaction dynamics is observed as a result of the interplay of the cavity parameters and phase difference. Actually, the CSs experience continuous phase shift due to self-phase and cross-phase modulation. In-phase CSs attract each other, while out-of-phase CSs repel. The initial phase difference influences the interaction dynamics significantly as portrayed in Fig. 17. While most of the initial phase difference (between the CSs) yield colliding CSs [Figs. 17(a)–17(c)], with certain initial phase differences [e.g., π in Fig. 17(d)], a CS drives the other one to a particular direction. This type of all-optical “pushing” of CSs was first reported in Ref. [12] and was called an “all-optical push-broom.” This push-broom effect can be controlled by the gradient in system parameters and by the

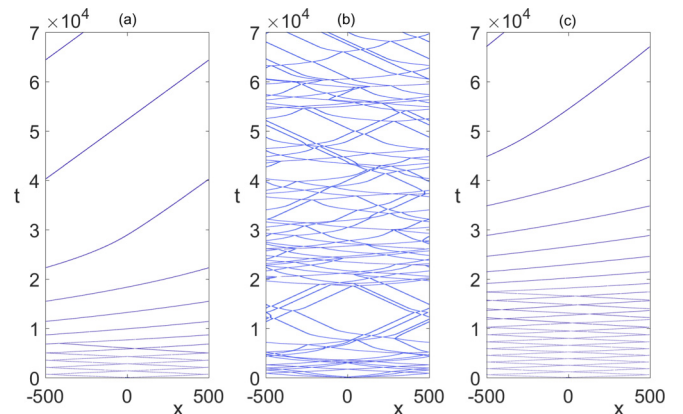


FIG. 16. Evolution of CS at optical communication wavelength 1550 nm with single initial pulse using GFSA as (a) active layer at $\sigma = 0.6$, (b) passive layer at $\sigma = 0.5$, and (c) active-passive layer at $\sigma = 0.55$. The rest of the parameters are kept the same as in Fig. 10.

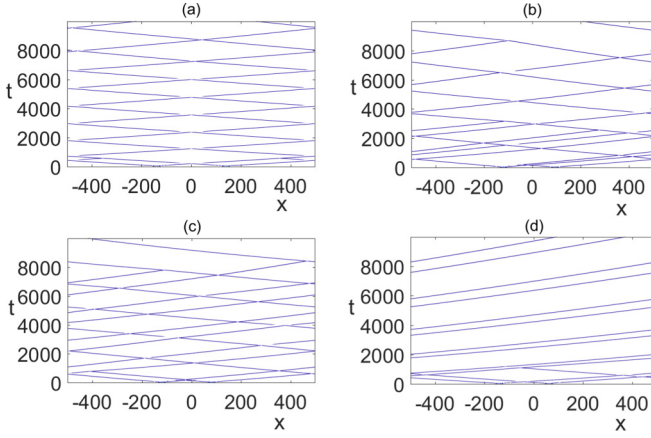


FIG. 17. Interaction dynamics of two CS at optical communication wavelength 1550 nm with GFSA as active-passive layer. The initial phase difference is (a) zero (b) $\frac{\pi}{4}$, (c) $\frac{\pi}{2}$, and (d) π . Here $\sigma = 0.55$ and the rest of the parameters are kept the same as in Fig. 10.

gradient of the writing beam; the latter promise more external control of CSs.

VIII. CONCLUSION

CS and CS molecules are excited in the heretofore unexplored visible as well as ultraviolet regions by replacing the common SESAM with a GFSA layer in the microresonator of a VCSEL that is coupled with a FSF. This immediately opens huge opportunity of CS applications in manifold wider operating regimes. Owing to the intrinsic properties of GFSA, CSs are generated at lower saturation intensity with a faster recovery of the VCSEL. Uses of GFSA as the only active medium and the only passive medium yield quite distinctive CS behavior. The CS dynamics of the former medium looks promising. When both active and passive media are GFSA, the behavior of the active medium still dominates. The gradient-induced spontaneous dynamics, two-CS interaction-dynamics, and the phase-induced dynamics all have the potential use in all-optical surface as well as bulk scanning. The broadband compatibility of GFSA gives an edge to such dynamics. The outcome of this investigation can be further used for experimental realization of broadband CS and CS molecule.

ACKNOWLEDGMENTS

J.K.N. would like to thank SPMS and TIET for providing financial support through a teaching assistance position. S. J. acknowledges the financial help of SERB, Govt. of India, through a Core Research Grant (File No. CRG/2019/005073). S. J. also acknowledges the financial support of Ministry of Electronics & Information Technology, MeitY, Govt. of India through a “Young Faculty Research Fellowship under Visvesvaraya Ph.D. Scheme” [Ref. No. MLA/MUM/GA/10(37) B]. S. J. would like to thank Prof. W. J. Firth and Dr. K. Nakeeran for their guidance and support.

APPENDIX: DERIVATION OF CGLE (10) FOLLOWING THE GENERIC WAY SHOWN IN REF. [43]

The dynamics of the cavity field in VCSELs embedded with graphene flake saturable absorber and coupled with FSF is governed by a system of equations as

$$\frac{\partial E}{\partial t} = [-(1 - i\theta) + (1 - i\alpha)d_a + (1 - i\beta)d_p + \alpha_{ns} + i\Delta]E + F, \quad (\text{A1})$$

$$\frac{\partial d_a}{\partial t} = -c_a[d_a\sqrt{1 + g_1|E|^2} - \mu], \quad (\text{A2})$$

$$\frac{\partial d_p}{\partial t} = -c_p[d_p\sqrt{1 + sg_2|E|^2} + \gamma], \quad (\text{A3})$$

$$\frac{\partial F}{\partial t} = -(\lambda + i\Omega_0)F + \sigma\lambda E. \quad (\text{A4})$$

For details please see the main text. Now we derive the expression for d_a from its corresponding rate equations (2) as (henceforth we substitute $|E|^2 = I_0$)

$$d_a = \left[1 - \frac{1}{c_a\sqrt{1 + g_1I_0}} \frac{\partial}{\partial t}\right]^{-1} \frac{\mu}{\sqrt{1 + g_1I_0}}. \quad (\text{A5})$$

Using a Taylor-series expansion, we get

$$d_a = \left[1 + \frac{1}{c_a\sqrt{1 + g_1I_0}} \frac{\partial}{\partial t} - \frac{1}{c_a^2(1 + g_1I_0)} \frac{\partial^2}{\partial t^2} + \dots\right] \times \frac{\mu}{\sqrt{1 + g_1I_0}}. \quad (\text{A6})$$

Considering the first term and neglecting the higher-order terms we get

$$d_a = \frac{\mu}{\sqrt{1 + g_1I_0}}. \quad (\text{A7})$$

In a similar way, the rate equation of carrier density d_p for a passive medium can be solved to reveal d_p as

$$d_p = -\frac{\gamma}{\sqrt{1 + sg_2I_0}}. \quad (\text{A8})$$

Employing a similar procedure, the expression for feedback strength can be acquired from its corresponding rate equation as

$$F = \left[1 + \frac{1}{\lambda + i\Omega_0} \frac{\partial}{\partial t}\right]^{-1} \frac{\sigma\lambda}{\lambda + i\Omega_0} E. \quad (\text{A9})$$

Applying a Taylor-series expansion, we get

$$F = \left[1 + \frac{1}{\lambda + i\Omega_0} \frac{\partial}{\partial t} - \frac{1}{(\lambda + i\Omega_0)^2} \frac{\partial^2}{(\partial t)^2} + \dots\right] \times \frac{\sigma\lambda}{\lambda + i\Omega_0} E. \quad (\text{A10})$$

Ignoring the higher-order terms, we get

$$F = \frac{\sigma\lambda}{\lambda + i\Omega_0} E = \left(\frac{\sigma\lambda^2}{\lambda^2 + \Omega_0^2} - i\frac{\sigma\lambda\Omega_0}{\lambda^2 + \Omega_0^2}\right) E \equiv (a - ib)E. \quad (\text{A11})$$

Now, substituting the expressions for d_a , d_p , and F , from Eqs. (7), (8), and (11) into Eq. (1) we get the required CGLE as

$$\frac{\partial E}{\partial t} = \left[-(1 - i\theta) + \mu \left(\frac{1 - i\alpha}{\sqrt{1 + g_1 I_0}} \right) - \gamma \left(\frac{1 - i\beta}{\sqrt{1 + sg_2 I_0}} \right) + \alpha_{ns} + i\Delta \right] E + (a - ib)E$$

-
- [1] T. Ackeman, W. J. Firth, and G. L. Oppo, *Adv. At. Mol. Opt. Phys.* **57**, 323 (2009).
- [2] S. Barbay, R. Kuszelewicz, and J. R. Tredicce, *Adv. Opt. Technol.* **2011**, 628761 (2011).
- [3] F. Leo, S. Coen, P. Kockaert, S.-P. Gorza, P. Emplit, and M. Haelterman, *Nat. Photonics* **4**, 471 (2010).
- [4] W. J. Firth and G. K. Harkness, *Asian J. Phys.* **7**, 665 (1998).
- [5] Y. Tanguy, T. Ackemann, W. J. Firth, and R. Jäger, *Phys. Rev. Lett.* **100**, 013907 (2008).
- [6] M. Eslami, R. Kheradmand, and F. Prati, *Phys. Rev. A* **89**, 013818 (2014).
- [7] W. J. Firth, Theory of Cavity Solitons, *Soliton-Driven Photonics*, edited by A. D. Boardman and A. P. Sukhorukov (Kluwer Academic Publishers, London, 2001).
- [8] E. Kapon and A. Sirbu, *Nat. Photonics* **3**, 27 (2009).
- [9] K. Panajotov, R. Michalzik, and K. D. Choquette, *Adv. Opt. Technol.* **2012**, 234163 (2012).
- [10] C. Carlsson, A. Larsson, and A. Alping, *J. Lightwave Technol.* **22**, 1694 (2004).
- [11] S. Barland, J. R. Tredicce, M. Brambilla, L. A. Lugiato, S. Balle, M. Giudici, T. Maggipinto, L. Spinelli, G. Tissoni, T. Knoedl, and M. Miller, *Nature (London)* **419**, 699 (2002).
- [12] X. Hachair, S. Barland, L. Furfaro, M. Giudici, S. Balle, J. R. Tredicce, M. Brambilla, T. Maggipinto, I. M. Perrini, G. Tissoni, and L. Lugiato, *Phys. Rev. A* **69**, 043817 (2004).
- [13] M. Bache, F. Prati, G. Tissoni, R. Kheradmand, L. A. Lugiato, I. Protsenko, and M. Brambilla, *Appl. Phys. B* **81**, 913 (2005).
- [14] A. J. Scroggie, W. J. Firth, and G.-L. Oppo, *Phys. Rev. A* **80**, 013829 (2009).
- [15] B. Kaur and S. Jana, *J. Lightwave Technol.* **36**, 2463 (2018).
- [16] J. Hader, H. J. Yang, M. Scheller, J. V. Moloney, and S. W. Koch, *J. Appl. Phys.* **119**, 053102 (2016).
- [17] U. Keller, Recent developments in compact ultrafast lasers, *Nature (London)* **424**, 831 (2003).
- [18] U. Keller, K. J. Weingarten, F. X. Kartner, D. Kopf, B. Braun, I. D. Jung, R. Fluck, C. Honninger, N. Matuschek, and J. Aus Der Au, *IEEE J. Sel. Top. Quantum Electron.* **2**, 435 (1996).
- [19] Z. Luo, D. Wu, Bin Xu, H. Xu, Z. Cai, J. Peng, J. Weng, S. Xu, C. Zhu, F. Wang, Z. Sund, and H. Zhange, *Nanoscale* **8**, 1066 (2016).
- [20] Z. Qin, G. Xie, H. Zhang, C. Zhao, P. Yuan, S. Wen, and L. Qian, *Opt. Express* **23**, 24713 (2015).
- [21] J. Mohanraj, V. Velmurugan, and S. Sivabalan, *Opt. Mater. (Amsterdam, Neth.)* **60**, 601 (2016).
- [22] M. K. Kavitha and M. Jaiswal, *Asian J. Phys.* **25**, 809 (2016).
- [23] E. Hendry, P. J. Hale, J. Moger, A. K. Savchenko, and S. A. Mikhailov, *Phys. Rev. Lett.* **105**, 097401 (2010).
- [24] Z. Liu, X. Zhang, X. Yan, Y. Chen, and J. Tian, *Chin. Sci. Bull.* **57**, 2971 (2012).
- [25] C. A. Zaugg, Z. Sun, D. Popa, S. Milana, T. Kulmala, R. S. Sundaram, V. J. Wittwer, M. Mangold, O. D. Sieber, M. Golling, Y. Lee, J. H. Ahn, A. C. Ferrari, and U. Keller, in *CLEO: Science and Innovations: Optical Society of America, CWIG.4* (Optical Society of America, 2013).
- [26] S. Husaini and R. G. Bedford, in *Proc. of the Vertical External Cavity Surface Emitting Lasers (VECSELs) IV: International Society for Optics and Photonics* 8966, Vol. 896608 (SPIE, 2014).
- [27] G. Q. Xie, J. Ma, P. Lv, W. L. Gao, P. Yuan, L. J. Qian, H. H. Yu, H. J. Zhang, J. Y. Wang, and D. Y. Tang, *Opt. Mater. Express* **2**, 878 (2012).
- [28] Z. Luo, M. Zhou, J. Weng, G. Huang, H. Xu, C. Ye, and Z. Cai, *Opt. Lett.* **35**, 3709 (2010).
- [29] J. E. Slagle, J. M. Murray, S. Guha, L. P. Gonzalez, and R. G. Bedford, *Appl. Phys. Lett.* **102**, 191112 (2013).
- [30] X. Li, Y. Tang, Z. Yan, Y. Wang, B. Meng, G. Liang, H. Sun, X. Yu, Y. Zhang, X. Cheng, and Q. Jie Wang, *IEEE J. Sel. Top. Quantum Electron.* **20**, 441 (2014).
- [31] A. Marini and F. J. Garcia de Abajo, *Phys. Rev. Lett.* **116**, 217401 (2016).
- [32] D. Popa, Z. Sun, F. Torrisi, T. Hasan, F. Wang, and A. C. Ferrari, *Appl. Phys. Lett.* **97**, 203106 (2010).
- [33] C. A. Zaugg, V. J. Wittwer, Z. Sun, D. Popa, S. Milana, T. S. Kulmala, R. S. Sundaram, M. Mangold, M. Golling, Y. Lee, J. H. Ahn, A. C. Ferrari, and U. Keller, in *Proc. of the Vertical External Cavity Surface Emitting Lasers (VECSELs) IV: International Society for Optics and Photonics* 8966, Vol. 896607 (SPIE, 2014).
- [34] B. V. Cunning, C. L. Brown, and D. Kielpinski, *Appl. Phys. Lett.* **99**, 261109 (2011).
- [35] Y. Tanguy, T. Ackemann, and R. Jäger, *Phys. Rev. A* **74**, 053824 (2006).
- [36] P. V. Paulau, D. Gomila, T. Ackemann, N. A. Loiko, and W. J. Firth, *Phys. Rev. E* **78**, 016212 (2008).
- [37] P. V. Paulau, D. Gomila, P. Colet, M. A. Matias, N. A. Loiko, and W. J. Firth, *Phys. Rev. A* **80**, 023808 (2009).
- [38] P. V. Paulau, D. Gomila, P. Colet, N. A. Loiko, N. N. Rosanov, T. Ackemann, and W. J. Firth, *Opt. Express* **18**, 8859 (2010).
- [39] C. Rimoldi, S. Barland, F. Prati, and G. Tissoni, *Phys. Rev. A* **95**, 023841 (2017).
- [40] C. Schelte, K. Panajotov, M. Tlidi, and S. V. Gurevich, *Phys. Rev. A* **96**, 023807 (2017).
- [41] W. J. Firth and P. V. Paulau, *Eur. Phys. J. D* **59**, 13 (2010).
- [42] P. V. Paulau, D. Gomila, P. Colet, B. A. Malomed, and W. J. Firth, *Phys. Rev. E* **84**, 036213 (2011).
- [43] L. Columbo, M. Piccardo, F. Prati, L. A. Lugiato, M. Brambilla, A. Gatti, C. Silvestri, M. Gioannini, N. Opačak, B. Schwarz, and F. Capasso, *Phys. Rev. Lett.* **126**, 173903 (2021) (Supplemental Material).
- [44] M. Piccardo, B. Schwarz, D. Kazakov, M. Beiser, N. Opačak, Y. Wang, S. Jha, J. Hillbrand, M. Tamagnone, W. T. Chen, A. Y. Zhu, L. L. Columbo, A. Belyanin, and F. Capasso, *Nature (London)* **582**, 360 (2020).

- [45] E. Yomba and T. C. Kofané, *Chaos, Solitons Fractals* **15**, 197 (2003).
- [46] W. P. Hong, *Z. Naturforsch.* **62a**, 368 (2007).
- [47] A. Mohamddou, A. K. Jiotsa, and T. C. Kofané, *Chaos, Solitons Fractals* **24**, 957 (2005).
- [48] S. Sahay, *Prog. Electromagn. Res. Lett.* **3**, 17 (2008).
- [49] M. Lakshmanan and S. Rajasekhar, *Nonlinear Dynamics* (Springer, Berlin, 2003).
- [50] G. J. de Valcarcel and K. Staliunas, *Phys. Rev. A* **87**, 043802 (2013).
- [51] S. Kumar, R. Herrero, M. Botey, and K. Staliunas, *Sci. Rep.* **5**, 13268 (2015).
- [52] R. Paschotta, R. Haring, A. Garnache, S. Hoogland, A. C. Tropper, and U. Keller, *Appl. Phys. B: Lasers Opt.* **75**, 445 (2002).
- [53] T. Ackemann, J. Jimenez, Y. Noblet, N. Radwell, G. Ren, P. V. Paulau, C. McIntyre, G. L. Oppo, J. P. Toomey, and D. M. Kane, in *Dynamics and Interaction of Laser Cavity Solitons in Broad-Area Semiconductor Lasers: Nonlinear Optical Cavity Dynamics*, edited by P. Grellu (Wiley-VCH Verlag GmbH & Co. KGaA, Weinheim, 2016).
- [54] J. Atai and B. A. Malomed, *Phys. Lett. A* **246**, 412 (1998).
- [55] B. A. Malomed and H. G. Winful, *Phys. Rev. E* **53**, 5365 (1996).
- [56] J. Atai and B. A. Malomed, *Phys. Rev. E* **54**, 4371 (1996).